The mixology of precursory strain partitioning approaching brittle failure in rocks

J. McBeck[1], Y. Ben-Zion[2], F. Renard[1,3]

1 Physics of Geological Processes, The Njord Centre, Department of Geosciences, University of Oslo, Norway
2 Department of Earth Sciences, University of Southern California, Los Angeles, CA, USA
3 Université Grenoble Alpes, Université Savoie Mont Blanc, CNRS, IRD, IFSTTAR, ISTerre, Grenoble, France

Abbreviated Title
The mixology of strain partitioning

Corresponding Author
J. McBeck
j.a.mcbeck@geo.uio.no

Summary

We examine strain accumulation and localization processes throughout twelve triaxial compression experiments on six rock types deformed in an X-ray transparent apparatus. In each experiment, we acquire 50-100 tomograms of rock samples at differential stress steps during loading, revealing the evolving 3D distribution of X-ray absorption contrasts indicative of density. Using digital volume correlation (DVC) of pairs of tomograms, we build time series of 3D incremental strain tensor fields as the rocks are deformed toward failure. The Pearson correlation coefficients between components of the local strain tensor at each stress increase step indicate that the correlation strength between local pairs of strain components, including dilation, contraction and shear strain, are moderate-strong in eleven of twelve experiments. In addition, changes in local strain components from one DVC calculation to the next show differences in the correlations between pairs of strain components. In particular, the correlation of local changes in dilation and shear strain is stronger than the correlation of changes in dilation-contraction and contraction-shear strain. In eleven of twelve experiments, the most volumetrically frequent mode of strain accommodation includes synchronized increase in multiple strain components. Early in loading, under lower differential stress, the most frequent strain accumulation mode involves the paired increase in dilation and contraction at neighboring locations. Under higher differential stress, the most frequent mode is the paired increase in dilation and shear strain. This mode is also the most or second most frequent throughout each complete experiment. Tracking the mean values of the strain components in the sample and the volume of rock that each component occupies reveals fundamental differences in the nature of strain accumulation and localization between the volumetric and shear strain modes. As the dilative strain increases in magnitude throughout loading, it tends to occupy larger volumes within the rock sample and thus delocalizes. In contrast, the increasing shear strain components (left- or right-lateral) do not necessarily

occupy larger volume and involve localization. Consistent with these evolutions, the correlation length of the dilatational strains tends to increase by the largest amounts of the strain components from lower to higher differential stress. In contrast, the correlation length of the shear strains does not consistently increase or decrease with increasing differential stress.

Keywords: Creep and deformation; Fracture and flow; Fault zone rheology; Dynamics and mechanics of faulting; Fractures, faults and high strain deformation zones

1. Introduction

Recognizing precursory signals approaching the onset of macroscopic failure is a critical goal in rock mechanics. Experimental observations indicate that fracture coalescence leading to macroscopic failure occurs through the opening of individual fractures that interact to allow shear deformation on a macroscopic scale (e.g., *Peng & Johnson*, 1975; *Petit & Barquins*, 1988; *Moore & Lockner*, 1995). Consequently, much previous work has highlighted the importance of dilation as a precursor to brittle failure (e.g., *Brace et al*., 1966). Although coalescing fractures may accommodate both opening and shearing, much research has focused on the dilatational rather than the shear deformation. This focus likely occurred because previous studies could not readily quantify the magnitudes of local dilation and shear strain operating within intact material or along individual fractures. Because the contribution of local dilation can influence the macroscopic expression of radial dilation, density, and seismic velocities in expected ways, the impact of local dilatational events could be estimated (e.g., *Bridgman*, 1949; *Handin et al*., 1963; *Frank*, 1965; *Brace et al*., 1966; *Myachin et al*., 1971). Far more limited analyses have quantified local deformation mechanisms that accommodate shear strain in triaxial experiments within intact rock by resolving the source types of acoustic emission events (e.g., *Stanchits et al*., 2006) and tracking macroscopic stress-strain relations, seismic anisotropy, and nonlinear resonance during deformation (e.g., *Hamiel et al.*, 2004a; 2009; *Lyakhovsky et al*., 2009).

Here, we characterize the strain accumulation and localization processes as rocks approach macroscopic failure, and compare the importance of contraction, dilation and shear strain in accommodating brittle deformation at varying stages of deformation. We analyze results from twelve triaxial compression deformation experiments on six rock types with an X-ray transparent deformation apparatus. In each experiment, we compress the rock core in stress steps and acquire a 3D tomogram at each step, revealing the 3D distribution of X-ray

absorption. Digital volume correlation (DVC) analysis implemented in the code TomoWarp2 (*Tudisco et al*., 2017) provide the 3D displacement vectors between tomogram acquisitions. From the time series of displacement fields, we calculate the contracting, dilating and shearing components of the strain tensor. From the time series of strain fields, we quantify how the incremental volumetric and shear strain components evolve during the approach to macroscopic failure.

This dataset enables comparing the strain localization and accumulation process in experiments on sandstone, basalt, monzonite, granite, shale, and limestone. We quantify the spatial correlation between each strain component, such as dilation and shear strain, and systematically compare the evolving correlations among pairs of strain components as well as different experiments and rock types. We track the strength of the strain accumulation process with the mean value of the strain component in each DVC calculation. We track the localization of the strain field using the volume of rock that the strain component occupies in each DVC calculation. We compare the accumulation and localization process for the volumetric strain components (dilation and contraction) and shear strain components (left- or right-lateral). We track the correlation length of each of the strain components in order to assess the growing (or shrinking) interaction distance of each strain component. The results provide novel descriptions of the strain accommodation and localization process in brittle rocks when approaching failure under upper crust conditions.

2. Brittle failure processes in rocks

Characterizing the micromechanical processes that produce brittle failure began with theoretical solutions for the stress field surrounding circular and elliptical holes (*Kolosov*, 1909; *Inglis*, 1913). *Griffith* (1921) initiated the field of Linear Elastic Fracture Mechanics (LEFM) by developing an energy-based condition for fracture propagation that lead to the

concept of the stress intensity factor, K, at a fracture tip (*Irwin*, 1948). Then, the stress field surrounding a crack tip could be approximated from the loading and stress intensity factors associated with tensile and shear fractures (e.g., *Lawn*, 1993). There are several well-recognized limitations of this seminal work. The analytical formulations predict unbounded stresses at the crack tip because LEFM formulations do not incorporate inelastic deformation beyond a stress threshold. Fracture mechanics models that include inelastic deformation in a process zone that eliminate crack tip singularities (e.g., *Rice*, 1980) help to address this limitation. Moreover, these analytical formulations predict the stress field surrounding a fracture tip and the likelihood of fracture propagation in systems with only one preexisting fracture or weakness that is much larger than other flaws in the system.

The Mohr-Coulomb failure criterion provides a macroscopic approach to understand brittle failure (*Coulomb*, 1776; *Mohr*, 1900), in contrast to the fracture-local, stress intensity factor approach. This failure criterion uses the stress state and material properties of the rock to predict whether and at what orientation a new fault develops, or whether slip occurs along a preexisting fault plane. Under low compressive stresses, these predictions statistically match observations (e.g., *Mitra*, 1994; *Storti et al*., 1997; *Crider & Pollard*, 1998; *McBeck et al*., 2017). But under tensile conditions, the theoretical uniaxial tensile strength derived from this criterion tends to exceed experimental measurements (e.g., *Paul*, 1961). The breakdown of the Mohr-Coulomb failure criterion in the tensile range leads to using two sets of failure criteria depending on whether the deformation is assumed to be dominated by tensile or shear deformation. These two sets of criteria produce, in turn, two different sets of stress thresholds for failure in tension or shear, and two sets of predicted fracture geometries (e.g., *Cooke & Madden*, 2014).

Dynamic instabilities that produce macroscopic events may be analyzed be examining the conditions leading to localization (*Rudnicki & Rice*, 1975; *Rice & Rudnicki*, 1980;

Lyakhovsky et al., 1997, 2011). Localization may occur at the critical conditions when the continuum equations of the increments of deformation lose ellipticity, or when the strain energy function of the material loses convexity. These and other analytical formulations are based on homogeneous solids, and so do not provide testable predictions about the precursors to macroscopic failure. Consequently, they do not provide insight into how to recognize the approach to brittle instabilities and macroscopic failures. Rock deformation experiments under triaxial compression show that systematic precursors to rock failure are detectable, at least in the laboratory (e.g., *Reches & Lockner*, 1994).

One of the most recognized precursors to failure in laboratory experiments is the macroscopic dilation of the rock sample. Monitoring the macroscopic axial and transverse strain of deformed rocks indicates that low porosity crystalline rocks dilate as they are compressed (e.g., *Brace et al*., 1966). The evolving reduction of seismic wave velocities and increasing V_p/V_s ratios in experiments provides evidence for dilation as increasing volumes of air- or water-filled fractures develop (*Nur*, 1972). Resolving the source types of acoustic emission events (e.g., *Stanchits et al*., 2006) further supports the concept that local tensile failure produces opening-mode deformation that leads to macroscopic dilation, as inferred from changes in the macroscopic strain and seismic velocities. Categorizing acoustic emissions into tensile events and mixed-mode or shear events during brittle deformation indicates that tensile failure can dominate the early deformation process, and that increasing proportions of mixed-mode and shear events occur toward failure (e.g., *Stanchits et al*., 2006; *Rodríguez & Celestino*, 2019). These works highlight that rock failure includes a mixture of deformation modes. Moreover, both the criteria used for tensile failure (Griffith) and shear failure (Mohr-Coulomb) do not consider volume changes in their original formulations, although some recent analyses have worked to incorporate dilation into the Mohr-Coulomb framework (e.g., *Hamiel et al*., 2005; *Zhao & Cai*, 2010).

Deriving the source type of acoustic emissions indicates that compactive mechanisms can comprise 5-15% of the deformation mode in both granite and basalt, even under low differential stress (20 MPa) (*Stanchits et al*., 2006). Cataclastic deformation bands with lower porosity than the surrounding rock (*Aydin & Johnson*, 1983) provide further evidence of local compaction as a dominant deformation mechanism. In porous rocks like basalt, sandstone and limestone that experience pore-collapse, local compaction may accommodate a greater proportion of the deformation than shear or dilation under certain stress conditions (e.g., *Huang et al.,* 2019). Theoretical work that describes the conditions of pore collapse, such as the Hertzian fracture concept, focus on the local stress concentrations that develop at the edges of pores and between grains (e.g., *Wong et al*., 1997). Consequently, several diverging failure criteria describe the conditions of compactive, tensile, and shear failure, although field and experimental evidence indicate that deformation occurs through the mixture of these modes.

Experimental data from *in situ* X-ray microtomography experiments on rocks under triaxial deformation can provide key observations on the importance of dilatational, contractive and shear deformation mechanisms in different rocks under various stress and temperature conditions. Microtomography scans image the 3D distribution of density contrasts produced by opening or closing fractures and pores, and minerals and rock fragments of different densities. Patterns of grey-level values that arise from density contrasts enable DVC on pairs of microtomography scans. DVC on pairs of scans acquired throughout triaxial rock deformation provide a time series of the 3D incremental strain tensor at varying differential stresses. The evolving statistics of the populations of dilatational, contractive and shear strains throughout the triaxial deformation enable comparing the relative importance of these deformation modes among different rock types.

158 DVC analysis on Fontainebleau sandstone (*Renard et al*., 2019a) and Mount Etna basalt
159 (*McBeck et al*., 2019) indicate that shear and dilation dominated the deformation process in
160 these porous rocks under low confining stress (10-20 MPa). The mean of the dilatational
161 strain population increased by larger magnitudes than the shear strain throughout these
162 experiments, suggesting the greater importance of the micromechanisms that produce local
163 dilation rather than shear. Tracking the 2D strain field on the surface of Carrara marble loaded
164 in uniaxial compression also reveals the dominance of shear and dilatational strain events
165 throughout loading, with a greater frequency of dilatational events near macroscopic failure
166 (*Tal et al*., 2016). DVC analyses on laminated Green River shale (*McBeck et al*., 2018)
167 provide a different partitioning of the strain modes than observed in the experiments on
168 marble, sandstone and basalt. In two experiments on shale, the magnitude of radial dilation
169 was of the same order as the magnitude of axial contraction throughout loading (*McBeck et*
170 *al*., 2018). Numerical modeling and the spatial distribution of localizing strain fields suggest
171 that localized contraction within a subhorizontal volume promotes shear strain localization
172 that leads to macroscopic failure of the rock (*McBeck et al*., 2018). The varying partitioning
173 of the strain modes in these different rock types prompts the current investigation of strain
174 partitioning in six different rock types throughout twelve experiments.
175 The present work quantitatively compares the relative contribution of contraction, dilation
176 and shear strain in triaxial deformation experiments on sandstone, basalt, monzonite, granite,
177 shale and limestone. This work examines the synchronicity of the strain accumulation and
178 localization process by finding the volume of rock occupied by increasing values of one, two
179 or three of the strain modes at each stage of each experiment. The study links the strain
180 accumulation (changing magnitude) and strain localization (changing volume) processes in
181 the (contractive and dilative) volumetric and (left- and right-lateral) shear strain modes. The
182 results may help to determine the appropriate failure criterion to use when predicting rock

failure in varying differential stress conditions. The results may also help to indicate whether different rock types require different failure criteria to robustly predict the onset of macroscopic failure.

3. Methods

3.1. In situ X-ray tomography experiment conditions

We deform rocks in the X-ray transparent deformation apparatus, HADES (*Renard et al*., 2016) installed on beamline ID19 at the European Synchrotron and Radiation Facility. The rock samples are cylinders 1 cm tall and 4-5 mm wide (**Table** 1). In each experiment, we increase the axial stress in steps of 0.5-5 MPa under constant confining stress between 5-35 MPa (**Table** 1) until the sample fails macroscopically. At each stress step, we acquire a 3D X-ray tomogram at 6.5 μm per voxel-side resolution while the sample is under constant load inside the deformation apparatus. Each scan requires about 2 minutes, and the final scan immediately precedes the macroscopic rock failure. Due to the stress-controlled loading, the rock cores fail with a rapid stress drop that prohibits imaging the rock as it supports decreasing axial stress.

These experiments have been described in previous studies from our group, including the experiments on Green River shale (*McBeck et al*., 2018), Fontainebleau sandstone (*Renard et al*., 2019a), monzonite (*Renard et al*., 2017, 2019b), Etna basalt (*McBeck et al*., 2019) and Anstrude limestone (*Renard et al*., 2017). The X-ray microtomography data for many of these experiments are available to the community (*Renard*, 2017, 2018a,b,c; *Renard & McBeck*, 2018).

3.2. Digital volume correlation

The DVC calculations are performed using the code TomoWarp2 (*Tudisco et al*., 2017). The DVC method searches for similar patterns of voxels in pairs of 3D volumes. The

parameters of the DVC calculation are constant in each experiment, with 20 voxel node spacing (0.13 mm) and 10 voxel correlation window size. The node spacing determines the spatial resolution of the calculation. The correlation window size determines the volume of the cube used to identify similar patterns of voxels. Both of these parameters can influence the magnitude of the strain calculated with DVC (*McBeck et al*., 2018), so we keep the parameters constant in each experiment.

For each experiment, ten DVC calculations are performed using scans separated by approximately equal increments of axial strain, producing ten incremental displacement fields between pairs of tomograms (**Figure** 1). The DVC calculations track the 3D displacement field between each scan acquisition, so the displacement vectors reflect the incremental deformation between the stress steps and not the cumulative deformation. Consequently, the incremental strain tensors calculated from these displacement fields quantify the incremental strain between each scan acquisition and not the cumulative strain.

From these displacement fields, we calculate the divergence and curl at each point of the DVC calculation (**Figure** S1). Negative and positive values of divergence indicate contractive and dilative strains, respectively. Negative and positive values of curl indicate the left-lateral and right-lateral shear strains, respectively. In order to compare the magnitude of the strain components throughout each experiment, we normalize the components by the macroscopic axial strain between each scan used in the DVC calculation, following the procedure of *McBeck et al*. (2018). This normalization aids comparison of the magnitude of the strain components at different stress steps in an experiment. Larger increments of imposed macroscopic axial strain will likely produce larger magnitudes of local strain than smaller increments, so normalizing the local strains by the magnitude of these increments helps reduce the impact of these varying magnitudes.

3.3. Experimental rock types

We focus on the deformation processes throughout twelve experiments on six rock types in this contribution, with two experiments on each rock type. Fontainebleau sandstone is a quartz arenite with a homogeneous mineralogical composition, well-sorted grain size distribution, average grain diameter of 0.25 mm, and 3-30% porosity (*Bourbie & Zinszer*, 1985). Mount Etna basalt is a porphyritic intermediate alkali basalt that experienced quick cooling, producing pores and thermal-induced fractures (*Vinciguerra et al*., 2005; *Benson et al*., 2007; *Heap et al*., 2009). Westerly granite is a crystalline intrusive igneous rock composed of about 40% plagioclase, 25% alkai feldspar, 29% quartz, and minor amounts of biotite, muscovite and chlorite (*Rutter & Neumann*, 1995). Monzonite is a crystalline intrusive igneous rock, and the monzonite deformed here has a mean grain size of 450 μm, and contains 18% quartz, 13% biotite, 58% plagioclase, 12% clinopyroxene and minor minerals (*Aben et al*., 2016). We deformed cores from the organic rich (R-8 unit) Green River shale that includes lacustrine marl/silt sediments that form laminations with 9.9 wt % organic matter (*Kobchenko et al*., 2011). The layering (laminations) of the Green River shale cores were set parallel to the maximum compression direction in these experiments. Anstrude limestone is an oolitic limestone that is nearly monomineralic with 98% calcite (*Han et al*., 2016). The sandstone, basalt and limestone cores had initial porosities of 5-7% (measured with imbibition and tomography data), 3% (measured with tomography data) and 4-8% (measured with tomography data), respectively. The initial porosities of the other rocks were below 0.5% as calculated with the tomography data.

4. Results

4.1. Correlating strain modes throughout loading

The spatial distribution of strain components with high magnitudes provides insights into the strain accumulation and localization processes within the rocks. **Figure** 2 shows the

location of high magnitudes (>90th percentile) of dilation, contraction and shear strain in the first DVC calculation, at the onset of loading under low differential stress, σ_D, and in the final DVC calculation, immediately preceding macroscopic failure and under higher σ_D. In the majority of the experiments, the strain fields are localized close to failure, but the granite and shale experiments do not reveal localization immediately prior to macroscopic failure (**Figure** 2d, e). The strain fields may not show localization because the macroscopic failure of the sample does not include localization and/or the localization occurs at a spatial or temporal resolution below those of the DVC calculations.

Among the experiments that show localization prior to failure, some components of the strain field appear spatially correlated with each other. In the sandstone and basalt experiments, high magnitudes of shear strain develop near high magnitudes of dilation. In contrast, in the monzonite and limestone experiments, high magnitudes of shear strain and dilation develop far from each other in some portions of the core. In the monzonite experiment, localized shear strain develops without accompanying dilation in the final DVC calculation (**Figure** 2c). In the limestone experiment, localized dilation develops in the upper portion of the core without localized shear strain (**Figure** 2f).

Following these observations, we calculate the Pearson correlation coefficient, ρ, between the strain components within subvolumes throughout pairs of scans, and throughout the time of the experiment. This calculation quantifies the spatial relationship between the strain components observed qualitatively in **Figure** 2. In particular, we compare the mean of each strain component magnitude within each sub-cube in a 3D grid separated by 0.2 mm, and thus with 0.2^3 mm^3 volume each, about twice the spatial resolution of the DVC calculation (0.13 mm) (**Figure** S1). The correlation coefficients thus track the similarity and differences in strain components within each sampling sub-cube of 0.2^3 mm^3 volume. We only report the correlation coefficients that are statistically significant, with p-values <0.05. Positive

283 correlations between strain components indicate that high magnitudes of one component are
284 associated with high magnitudes of the other component. Negative correlations indicate that
285 high magnitudes of one component are associated with low magnitudes of the other
286 component. Values of the correlation coefficient, $|\rho|$, <0.3 indicate weak correlations,
287 between 0.3 to 0.5 indicate moderate correlations, and $|\rho|$>0.5 indicate strong correlations
288 (e.g., *Cohen*, 1988).

289 To examine the correlation between how each strain component evolves from one DVC
290 calculation to the next, we also calculate the change in the mean of each strain component
291 magnitude at each cube in the sampling grid, and calculate the correlation coefficient between
292 the changes in the means. We do not consider the difference between left- and right-lateral
293 shear strains in this analysis, and perform the correlation calculations using the absolute value
294 of the shear strain. In summary, we report the correlation between the magnitude of 1) the
295 mean dilation and mean contraction magnitude, 2) the mean dilation and mean shear strain
296 magnitude, 3) the mean contraction and mean shear strain magnitude, 4) the change in the
297 mean dilation and change in the mean contraction magnitude, 5) the change in the mean
298 dilation and change in the mean shear strain magnitude, and 6) the change in the mean
299 contraction and change in the mean shear strain magnitude (**Figure** 3).

300 Most of the correlations between the mean of the strain components (**Figure** 3a-b) are
301 positive in each experiment, except the shale experiment GRS03. This experiment hosts a
302 moderate-strong negative correlation between contraction and dilation, and contraction and
303 shear strain (**Figure** 3, **Figure** S2). In the other experiments, contraction and dilation have
304 moderate-strong positive correlations, and contraction and shear strain have weak-moderate
305 positive correlations. In experiment GRS03, in contrast, increasing contraction does not yield
306 higher magnitudes of dilation or shear strain (**Figure** S2).

Whereas the directions (positive or negative) and strengths of the correlations between the pairs of strain component means (**Figure** 3a-b) are similar in all but one experiment, the correlations between evolving changes of the mean of the strain component (**Figure** 3c-d) show greater differences. The correlations between the change in the dilation and contraction, and contraction and shear strain are near zero or negative with weak strength. In contrast, the correlation between the change in contraction and dilation are higher with moderate-strong positive correlations.

These varying signs of the correlation coefficients indicate that the strain accommodation process is dominated by the paired response of changes in dilation and shear strain throughout each experiment. Increasing changes in dilation are paired with increasing changes in shear strain. However, increasing changes in contraction are not strongly associated with increasing changes in shear strain or increasing changes in dilation. Whereas the magnitudes of these strain components (**Figure** 3a-b) are generally positively correlated with each other, the changes of evolving strain components are only positively correlated for the paired dilation-shear strain, and not for dilation-contraction and contraction-shear strain.

4.2. Volumetric frequency of strain accommodation modes

The observed differences in the correlation coefficients between changes in the mean strain component magnitude prompt a more detailed investigation into the spatial distribution of the modes of strain accommodation. Here, we examine the relative volumes of rock that experience various strain accommodation modes, including the paired increase in dilation and shear strain, the paired increase in contraction and shear strain, and the paired increase in contraction and dilation in individual subvolumes throughout the rock cores (**Figure** 4). We also report how this partitioning evolves from lower to higher differential stress conditions. We document the relative fraction rock volume that experienced these varying strain combinations, as measured with the number of cubic subvolumes that experienced different

strain combinations. These sampling subvolumes are the same as used in the analysis of **Section** 4.1.

Throughout the full experiment, the most volumetrically frequent mode of strain accommodation is the paired increase in the mean of dilation and shear strain (within the same subvolume) in all but the granite experiment (WG04) (**Figures** 4a, S3). Even in experiment WG04, this mode of strain accommodation is the second most frequent, after the increase in shear strain (**Figures** S3, 4). The increase in the mean of only the shear strain is typically the second or third most frequent strain accommodation mode in all experiments (**Figures** S3, 4).

The nature of strain accommodation at the first (**Figure** 4b) and final (**Figure** 4c) experimental stages captured in the DVC calculation shows that the most frequent mode of strain accommodation evolves from lower to higher differential stress conditions. Early in loading, the paired increase in contraction and dilation is generally one of the most frequent modes. This mode of strain accommodation is the most frequent in the experiments on basalt, monzonite and granite, and the second most frequent in the experiments on sandstone and shale in the first DVC calculation. In the limestone experiments, the most frequent mode in this early stage is the increase in only the shear strain.

Immediately preceding macroscopic failure, the paired increase in dilation and shear strain is one of the most frequent modes, as well as the increase in only shear strain (**Figure** 4c). The paired increase in dilation and shear strain is the most frequent mode in the basalt, monzonite, granite and shale experiments at this stage. This mode is the second most frequent in the sandstone and limestone experiments preceding failure. The most frequent mode in the sandstone and limestone experiments is the lone increase in shear strain, and the decrease in all of the strain components, respectively.

4.3. Comparing strain accumulation and localization

357 The previous analyses link the spatial coincidence of different strain components, and
358 compare the evolution of this coincidence from lower and higher differential stress
359 conditions. The differences in this evolution with differential stress prompt an examination of
360 the strain accommodation mode throughout each experiment with a higher temporal
361 resolution. In particular, we track the mean amplitude and rock volume occupied by four
362 strain components: dilation, contraction, left-lateral shear strain and right-lateral shear strain
363 at each DVC calculation (**Figures** 5, S4, 6). Previous work indicates that the evolution of the
364 rock volume occupied by dilation relative to contraction, and the volume occupied by left-
365 lateral relative to right-lateral shear strain, signal approaching macroscopic failure (*Renard et*
366 *al*., 2019b; *McBeck et al*., 2019).
367 We adopt the convention of showing when the dilation exceeds the contraction, and when
368 the left-lateral shear strain exceeds right-lateral shear strain (**Figures** 5, S4, 6). Because the
369 mean and volume of the dilation tend to increase, while those properties of the contraction
370 tend to decrease with loading, we mark the axial strain range when the dilation exceeds the
371 contraction. The axial strain range when the left-lateral shear strain exceeds the right-lateral
372 shear strain is no more significant than when the right-lateral shear strain exceeds the left-
373 lateral shear strain in our experiments. Marking the intervals when right-lateral shear strain
374 exceeds the left-lateral shear strain would produce the same patterns as found with the
375 adopted convention.
376 In all but one of the limestone experiments (ANS02), the mean of the dilation exceeds the
377 mean of the contraction at some stage (**Figures** 5, S4). Similarly, in all but this experiment,
378 the volume of rock occupied by dilation exceeds that occupied by contraction at some stage
379 (**Figures** 5, S4). Some of the experiments also show that the mean or volume of one of the
380 shear strain components exceeds the other for intervals of axial strain. In some experiments
381 (i.e., FBL01, GRS02, WG02) the axial strain interval over which the mean of the dilation

382 exceeds the mean of the contraction aligned with the axial strain interval over which the
383 volume occupied by the dilation exceeds the volume occupied by the contraction (**Figure** 5a,
384 d, e). In fewer experiments, the intervals over which both the mean and volume of left-lateral
385 shear strain exceeds the right-lateral shear strain coincide (i.e., FBL01, **Figure** 5a).
386 **Figure** 6 shows the experiment stages (macroscopic axial strain) over which the dilation
387 exceeds the contraction, and the left-lateral shear strain exceeds the right-lateral shear strain,
388 in terms of either the mean magnitude or volume. In all but one of the experiments (ANS02),
389 the normalized axial strain when the dilation first exceeds the contraction occurred at 0.3-0.7
390 axial strain from failure (**Figure** 6). In the limestone experiment ANS02, the volume and
391 mean of the contraction exceed those properties of the dilation throughout the full experiment,
392 consistent with the expected pore-collapse mechanism operating in limestone during brittle
393 failure (e.g., *Zhu et al*., 2010). In all of the experiments, the time when the mean dilation
394 exceeds the mean contraction overlaps the time when the volume occupied by dilation
395 exceeds the volume occupied by contraction. When higher magnitudes of dilation permeate
396 the rock, the dilative strains also occupy more volume than the contractive strains.
397 For most experiments (e.g., FBL02, MONZ05, GRS03), the timing of the shear strain
398 accommodation modes is not coincident. In these experiments, the mean of the left-lateral
399 shear strain exceeds the mean of the right-lateral shear strain throughout a time interval when
400 the volume occupied by the left-lateral shear strain does not exceed the volume occupied by
401 the right-lateral shear strain. Higher magnitudes of shear strain are not always (or often)
402 coincident with permeating larger volumes. The few experiments in which larger volumes of
403 left-lateral shear strain occur at the same axial strain ranges of larger means of left-lateral
404 shear strain include the sandstone experiment FBL01 and both basalt experiments.
405 To more directly compare the synchronicity of the strain accumulation and localization
406 processes, we report the percentage of the macroscopic axial strain (i.e., experimental time)

that both the mean and volume of one of the strain components (dilation or left-lateral shear strain) exceed the other component (contraction or right-lateral shear strain) (**Figure** 7). We report this percentage out of the total axial strain corresponding to the mean magnitude or fractional volume, whichever is longer (e.g., **Figure** 7a). In only one experiment (sandstone, FBL01), the percentage of overlap time when both the mean and volume of the left-lateral shear strain exceed the right-lateral shear strain is higher than the percentage of overlap time for the volumetric strains (**Figure** 7c). In seven experiments, the percentage of overlap time of the volumetric strains is higher than the overlap time of the shear strains. In three experiments, the overlap times of the volumetric and shear strains are similar. Grouping the overlap times by rock types (**Figure** 7b), and calculating the average of the overlap time of each pair of experiments on the same rock type, reveals that only the pair of experiments on sandstone have average overlap times of the shear strain that exceed the average overlap times of the volumetric strains. For all the other rock types, the average overlap times of the volumetric strains are higher than the average overlap times of the shear strains.

Increases in the magnitude of dilation generally are coincident in time with increases in the volume experiencing this dilation. In contrast, increases in the magnitude of shear strain are coincident with increases in the volume rock experiencing the strain with lower frequency than the volumetric strains. Whereas dilation tends to occupy larger volumes (delocalizing) as it gains strength throughout each experiment, shear strain tends to occupy the same or smaller volumes (localizing) as it gains strength.

4.4. Tracking the interaction distance of strain modes

Building on the previous observations, we now examine how the evolving local volumetric and shear strains influence the strain network within the entire rock sample throughout loading. We calculate the Pearson correlation coefficient between the same strain components at pairs of sub-volumes in the core with increasing distances at each differential

stress step. The distribution of correlation coefficients at each stress step evolves from one at zero distance (when the same sub-volumes are correlated to each other) to near zero at distances close to the diameter of the rock core (4 mm) (**Figure** S5). The correlation length is taken from the distribution of correlation coefficients as the distance at which the correlation coefficient decreases below 0.5. We track the correlation length in each experiment for the strain components of contraction, dilation, shear strain (including both the left- and right-lateral shear), and the separate left- and right-lateral shear strains. **Figure** S5 shows the distribution of correlation coefficients with distance for half of the experiments, with one example for each rock type, and the correlation lengths derived from these distributions of the five strain components. **Figure** 8 shows how the correlation lengths evolve with time (axial strain) for the set of experiments shown in **Figure** S5.

In some experiments, such as for sandstone and granite, the correlation lengths of the dilation, shear strain, and left-and right-lateral shear strains increase toward failure (**Figure** 8a, d). In other experiments, such as for basalt, these correlation lengths decrease toward failure (**Figure** 8b). In the monzonite experiment, the correlation lengths of each strain component increase somewhat throughout the loading (**Figure** 8c). The evolving correlation lengths of the shale and limestone samples do not show a systematic trend with loading. In these experiments, the correlation lengths of different strain components at a given stress step differ from each other by 0.5-2 mm. In contrast, in the other experiments, the correlation lengths of the dilation and shear strain components are more similar at a given stress step.

To compare the evolution of the correlation lengths across all 12 experiments, we show the correlation length at the first and final DVC calculation of each experiment, and the difference in the lengths between these times (**Figure** 9). In the first DVC calculation, under lower differential stress, the dilation tends to produce the lowest correlation length of the strain components for each rock type (**Figure** 9a,b). At this stage, the correlation lengths of

457 the contraction and shear strains tend to be similar to each other, and higher than the dilation.
458 In the final DVC calculation, under higher differential stress, the correlation length of the
459 contraction tends to be lower than the other strain components (**Figure** 9c,d). The correlation
460 length of the dilation tends to be larger than the contraction, and equal or greater than the
461 length of the shear strains. The difference in the correlation length between the first and final
462 DVC calculations shows that the dilation generally increases by the largest lengths throughout
463 loading (**Figure** 9e,f). In contrast, the contraction generally decreases in length with loading,
464 or remains at a similar value. The correlation length of the contraction tends to decrease with
465 loading for the sandstone, basalt, monzonite, and granite experiments, but stays at a similar
466 length for the shale and limestone experiments (**Figure** 9f). The change in the correlation
467 length with loading for the shear strain, and the individual left- and right-lateral shear strains
468 is on average near zero for the groups of rock types, but with ranges above and below zero by
469 up to 1 mm for each individual experiment. An analysis that accounts for correlations in
470 different directions, such as parallel and normal to the ultimate final failure zone, may provide
471 additional useful information, but is left for future work.
472 Tracking the change in the correlation length through time suggests that the dilatational
473 strain evolves from influencing the smallest volume of rock of the strain components under
474 lower differential stress to the largest volume of rock under higher differential stress. This
475 increasing interaction distance of the dilatational strain, and generally more limited interaction
476 distance of the shear strains, agrees with our observation that dilation tends to occupy larger
477 rock volumes when increasing in magnitude, whereas the shear strain occupies smaller
478 volumes (i.e., localizes) when increasing in magnitude (**Figures** 6, 7).
479

480 ## 5. Discussion

481 ### 5.1. Coincidence of strain modes

Digital volume correlation of tomography data acquired in twelve triaxial deformation experiments on six rock types reveal the interplay of local contraction, dilation and shear strain when approaching macroscopic failure. Our work indicates that the strain partitioning process in crustal rocks under the triaxial conditions of the upper crust is dominated by the synchronous expression of multiple strain modes (**Figures** 3-4, 10a). The strengths of local correlations between each pair of strain components in the examined sub-volumes are similar to each other (**Figure** 3). The link between shear strain and dilation has been well-recognized in the brittle failure of rocks under triaxial compression (e.g., *Hamiel et al*., 2004b, *Stanchits et al*., 2006; *Tal et al*., 2016; *McBeck et al*., 2019; *Renard et al*., 2019a,b), and shear strain associated with contraction has been recognized in fewer geologic systems such as cataclastic compaction band development (e.g., *Aydin & Johnson*, 1983). However, the co-existence of contraction and dilation in small sub-volumes has received less attention (e.g., *Renard et al*., 2019b). The similarity of the strengths of the correlations may occur because we track this correlation throughout triaxial loading, with increasing differential stress. The similar positive correlation strengths suggest that the different modes of strain play complementary roles during deformation. Loading accelerates the strain accumulation process, producing a synchronous increase in the magnitude of local contraction, dilation and shear strain.

The correlations in the changes of the strain components align with previous inferences about the link between dilation and shear strain, relative to contraction and shear strain (**Figure** 3). In particular, the strength of the correlation between the change in dilation and shear strain is higher than the correlation between the change in contraction and shear strain in all of the experiments. Discrete compaction bands do not develop in any of the experiments, so the link between contraction and shear strain is expected to be weak. When rough surfaces slip, they must either abrade existing asperities or dilate, producing the strong link between the change in dilation and shear strain (**Figure** 10a).

507 The most volumetrically frequent mode of strain accommodation throughout each
508 complete experiment is the paired increase in dilation and shear strain, and not the individual
509 increase in one of the strain modes, in eleven of twelve experiments (**Figure** 4). Under
510 relatively low differential stress, the most common strain accommodation mode is the paired
511 increase in dilation and contraction (**Figures** 4, 10b). The DVC analysis suggests that as
512 preexisting pores close due to increased axial and confining stress, they also dilate in volumes
513 near the contracting volumes (**Figure** 10b). The results agree with previous qualitative
514 observations of the spatial relationship between high magnitudes of dilation and contraction
515 recognized from DVC of X-ray tomography scans of monzonite (*Renard et al*., 2019b).
516 Earlier work has noted the tendency of porous rocks to macroscopically contract at the onset
517 of loading (e.g., *Brace et al*., 1966). First motion polarity analysis of acoustic emissions in
518 experiments on basalt and granite indicate that collapse-type events dominate deformation
519 under hydrostatic loading (*Stanchits et al*., 2006). Alternating increases and decreases in
520 gravity between flank eruptions on Mount Etna may have arisen from the opening of fractures
521 and local contraction, and not only from magma movement prior to failure (e.g., *Carbone et*
522 *al*., 2014).
523 Under higher differential stress, the most volumetrically common strain accommodation
524 mode is the paired increase in dilation and shear strain (**Figures** 4, 10b). The results indicate
525 that the dilation and shear strain magnitudes increase from one DVC calculation to the next
526 by similar magnitudes within each subvolume (**Figure** 3), and that this paired strain
527 combination occupies the largest volume within the rock out of all the possible strain
528 combinations (**Figure** 4). As mentioned, previous work has identified the importance of both
529 dilation and shear deformation in rock failure (e.g., *Stanchits et al*., 2006). This may arise
530 from micromechanical processes that include (1) the opening of smaller mode-I fractures that
531 link into through-going faults that accommodate shear strain detectable at the macroscopic

scale (e.g., *Petit & Barquins*, 1988; *Moore & Lockner*, 1995), (2) the propagation of tensile fractures aligned parallel to σ_1 that form columns of rock that rotate to allow macroscopic shear (e.g., *Peng & Johnson*, 1975), and/or (3) the opening of tensile fractures aligned parallel to σ_1 at the tips of wing-cracks inclined relative to σ_1 that accommodate slip (e.g., *Wong & Chau*, 1998). The spatial resolution of the DVC analyses presented here does not enable distinguishing between these different micromechanisms, but does indicate that these processes are consistent with the high volumetric frequency and strong positive correlation of the coeval development of dilation and shear strain.

The difference in the most volumetrically frequent strain accommodation mode from lower (contraction and dilation) to higher (dilation and shear strain) differential stresses suggest that different failure criteria may apply for local and macroscopic failures under these different stress conditions. Under lower differential stresses, criteria that describe the conditions of pore-collapse and tensile failure (e.g., *Wong et al*., 1997) may be the most successful at predicting local failure. Under higher differential stresses, criteria that incorporate micromechanisms that accommodate both dilation and shear (e.g., *Peng & Johnson*, 1975; *Petit & Barquins*, 1988; *Moore & Lockner*, 1995; *Wong & Chau*, 1998) may be the most successful for predicting progressive development of local processes that produce macroscopic failure. When considering the complete loading history of an experiment under triaxial compression, or progressively increasing differential stress in a volume of crust, criteria that involve the paired development of dilation and shear deformation may be most successful.

5.2. The relationship between strain accumulation and localization

Tracking the mean and the volume of rock occupied by each strain component in each DVC calculation reveals differences between the strain accumulation and localization processes of the volumetric and shear strains. These processes occur over longer periods of

time (i.e., macroscopic axial strain) for the local volumetric strains than the local shear strains. In all but one experiment, both the mean and volume of the dilatational strains exceed those of the contractive strains at some stage of the experiment. In particular, the mean and volume of the local dilation exceed those of the contraction between 0.3-0.7 normalized axial strain, with 1 being the axial strain at failure (**Figure** 6). For these experiments, the axial strain at which the mean dilation exceeds the mean contraction occurs close to when the volume occupied by the dilatational strains exceeds the volume occupied by the contractive strains (**Figure** 7). In contrast, the timing of when the mean of the left-lateral shear strain exceeds the mean of the right-lateral shear strain coincides with the trends in the volume occupied by the different shear strains over a shorter time period (**Figures** 6, 7). Whereas dilation tends to occupy larger volumes (delocalizing) as it increases in amplitude, the shear strain tends to occupy the same or smaller volumes (localizing) as it gains strength (**Figures** 7c, 10c). Tracking the correlation length of each of the strain components throughout loading supports these observations (**Figures** 8, 9). The correlation length of the dilation tends to increase by the largest magnitudes from lower to higher differential stresses, whereas the correlation lengths of the other components tend to change by lower magnitudes (**Figures** 8, 9). Throughout loading, the interaction range of dilation tends to increase, while this range tends to decrease or stay similar for the other strain components.

The differences between the evolution of the dilatational and shear strains are somewhat intuitive because dilatational strain involves volume change implicitly, but shear strain does not necessarily. However, the methods of calculating the volume occupied by each strain component and tracking the correlation length do not consider the change in volume produced by each deformation mode. These methods only consider the number of subvolumes that contain the expression of the strain mode, and the magnitude of the strain components in these subvolumes. These analyses demonstrate that the dilatational strain accumulation process

582 involves increases in volume within the subvolume of calculation, increases in the number of
583 subvolumes exhibiting dilation, and increases in the distance of the influence of dilation.
584 The development of networks of compaction bands may also produce a paired increase in
585 the magnitude of strain accommodated by the bands and the volume occupied by the bands
586 with increasing differential stress. *Mair et al*. (2000) documented that the total amount of
587 macroscopic axial strain accommodated by high porosity (20%) sandstone in triaxial
588 deformation experiments was linearly related to the number of compaction bands that
589 developed. If the amount of local strain accommodated by each band also increased with the
590 number of bands, then both the magnitude of local strain and volume experiencing this strain
591 would have increased, consistent with the trend observed in the DVC results. Interestingly,
592 this trend does not occur for only the experiments with sandstone, but in the experiments with
593 the other sedimentary rocks and low porosity crystalline rocks as well (**Figures** 6, 7).
594 Moreover, this trend may exist for the local contractive strains during compaction band
595 development (e.g., *Mair et al*., 2000), but the DVC calculations identify this trend in the
596 dilatational strain rather than the contractive strain in eleven of twelve experiments.
597 The eventual coalescence of many individual fractures into through-going faults produces
598 the observed paired increase in left- or right-lateral shear strain and decrease in the volume
599 occupied by that strain. Fault networks may evolve from distinct fracture segments that
600 propagate until they begin to interact and link with neighboring segments, ultimately forming
601 one or a few larger faults (e.g., *Mansfield & Cartwright*, 2001; *Ben-Zion & Sammis*, 2003;
602 *Crider & Peacock*, 2004; *Crider*, 2015; *Peacock et al*., 2018). The mean shear strain (in either
603 the left- or right-lateral direction) accommodated by each smaller fault segment at the
604 incipient stages of fault network development may be lower than the mean shear strain
605 accommodated by the more continuous fault strands that develop later. Similarly, the total
606 volume of the incipient fault segments could be higher than the total volume of the through-

going fault strands if some of the fault strands are abandoned as other segments link. Under ductile deformation conditions, the magnitude and volume of shear strain accommodated in a shear zone may show a similar behavior: increasing in magnitude while decreasing in volume. Over time, the effective width of a shear zone may decrease, increasing the shear strain accommodated along the zone, provided the amount the fault-plane parallel displacement remains similar or constant. In both the brittle and ductile realms, the shear strain accumulation and localization processes may evolve in opposite senses: increasing in magnitude while decreasing in volume (e.g., **Figure** 10c), as documented in our experiments.

6. Conclusions

Using twelve triaxial deformation X-ray tomography experiments on six rock types, we examine the strain accumulation and localization process as rocks are compressed toward failure. At these experimental conditions representing the upper crust (5-35 MPa confining stress), the strain accumulation process involves the paired increase in several components. The strengths of this paired increase of strain components, as measured with the Pearson correlation coefficient, are moderate-high in all but one experiment (**Figure** 3). The correlation between the *changes* in the dilation and shear strain from one tomogram to the next (or stress step) are stronger than the correlations between the changes in the (1) contraction and shear strain and (2) dilation and contraction. Tracking the volumetric frequency of strain components reveals that the most frequent mode of strain accommodation throughout each complete experiment is the paired increase in the dilation and shear strain in eleven of twelve experiments (**Figure** 4). Under low differential stress, the most volumetrically frequent mode of strain accommodation is the paired increase in dilation and contraction (**Figures** 4, S3, 10b). Under higher differential stress, the most volumetrically frequent mode of strain accommodation is the paired increase in dilation and shear strain

(**Figures** 4, 10b). Tracking the mean of each strain component and volume of rock occupied by the strain component reveals different behaviors of the volumetric and shear strains (**Figures** 5, 6, 7, S4). Whereas dilation tends to occupy larger volumes (delocalizing) as it gains strength, shear strain tends to occupy the same or smaller volumes (localizing) as it gains strength (**Figures** 7, 10c). Tracking the correlation distance for each of the strain components throughout loading shows that the interaction distance of the dilation grows larger from lower to higher differential stress than any of the other strain components, including the contraction and shear strains (**Figures** 8, 9, 10c). These observations provide constraints on the relevant failure criteria that describe the onset of localized failure, and the corresponding precursory signals. Successful macroscopic failure criteria should incorporate the paired response of dilation and shear strain to describe and predict the evolution toward failure. Future work may use the presented observations of the differing evolutions of magnitude, correlation length and volume occupied by the dilation and shear strain from lower to higher differential stress to assess the success of existing and new failure criteria. The observed trends in strain accumulation and localization tend to be consistent among the six rock types, suggesting that different rock types may not require different failure criteria. This idea suggests that a unified theory may be able to describe precursory strain localization leading to macroscopic failure in rocks of varying microstructure, porosity and composition.

Acknowledgements

The deformation apparatus was built by Sanchez Technology. Elodie Boller, Paul Tafforeau, and Alexander Rack provided advice on the design of the tomography setup. Stephen Hall and Erika Tudisco provided advice on the application of TomoWarp2. This study received funding from the Norwegian Research Council (project PROMETHEUS, grant 267775). Beamtime was allocated at the European Synchrotron Radiation Facility (Long Term

Proposal ES-295). Data storage was provided by UNINETT Sigma2 - the National Infrastructure for High Performance Computing and Data Storage in Norway (project NS9073K). The DVC data will be available on UNINET Sigma2 – the National Infrastructure for High Performance Computing and Data Storage in Norway upon publication of the present work.

References

Aben, F.M., Doan, M.L., Mitchell, T.M., Toussaint, R., Reuschlé, T., Fondriest, M., Gratier, J.-P., & Renard, F., 2016. Dynamic fracturing by successive coseismic loadings leads to pulverization in active fault zones, *J. Geophys. Res.: Solid Earth*. 121 (4), 2338–2360.

Aydin, A., & Johnson, A. M., 1983. Analysis of faulting in porous sandstones, *Journal of Structural Geology*, 5(1), 19-31.

Benson, P. M., Thompson, B. D., Meredith, P. G., Vinciguerra, S., & Young, R. P., 2007. Imaging slow failure in triaxially deformed Etna basalt using 3D acoustic-emission location and X-ray computed tomography, *Geophysical Research Letters*, 34, L03303. https://doi.org/10.1029/2006GL028721.

Bourbie, T., & Zinszner, B., 1985. Hydraulic and acoustic properties as a function of porosity in Fontainebleau sandstone, *J. Geophys. Res.*, 90(B13), 11524–11532.

Brace, W. F., Paulding, B. W., & Scholz, C. H., 1966. Dilatancy in the fracture of crystalline rocks, *J. Geophys. Res.*, 71(16), 3939-3953.

Bridgman, P.W., 1949. Volume changes in the plastic stages of simple compression. *Journal of Applied Physics*, *20*(12), pp.1241-1251.

Carbone, D., Aloisi, M., Vinciguerra, S., & Puglisi, G., 2014. Stress, strain and mass changes at Mount Etna during the period between the 1993-94 and 2001 flank eruptions. *Earth-Science Reviews*, 138, 454–468. https://doi.org/10.1016/j.earscirev.2014.07.004.

Cohen, J. (1988). Statistical power analysis for the behavioral sciences (2nd ed.). Hillsdale, NJ: Erlbaum.

Cooke, M.L. and Madden, E.H., 2014. Is the Earth lazy? A review of work minimization in fault evolution. *Journal of Structural Geology*, *66*, 334-346.

Coulomb, C., 1776. Sur une application des rêgles maximis et minimis à quelques problèmes de statique, relatives à l'architecture, *Acad. Sci. Paris Mem. Math Phys*., 7:343–382.

687 Crider, J.G., 2015. The initiation of brittle faults in crystalline rock. *Journal of Structural*
688 *Geology*, *77*, 159-174.

689 Crider, J.G., & Peacock, D.C., 2004. Initiation of brittle faults in the upper crust: a review of
690 field observations. *Journal of Structural Geology*, *26*(4), 691-707.

691 Crider, J.G., & Pollard, D.D., 1998. Fault linkage: Three-dimensional mechanical interaction
692 between echelon normal faults. *J. Geophys. Res.: Solid Earth*, *103*(B10), 24373-24391.

693 Frank, F.C., 1965. On dilatancy in relation to seismic sources. *Reviews of Geophysics*, *3*(4),
694 485-503.

695 Griffith, A. A., 1921. The phenomena of rupture and flow in solids, *Philosophical*
696 *Transactions of the Royal Society of London Series A*, 221(582-593), 163-198.

697 Hamiel, Y., Liu, Y., V. Lyakhovsky, Y. Ben-Zion and D. Lockner, 2004a. A Visco-Elastic
698 Damage Model with Applications to Stable and Unstable fracturing, *Geophys. J. Int.*, 159,
699 1155-1165, doi: 10.1111/j.1365-246X.2004.02452.x.

700 Hamiel, Y., Lyakhovsky, V., & Agnon, A., 2004b. Coupled evolution of damage and porosity
701 in poroelastic media: theory and applications to deformation of porous rocks. *Geophys. J.*
702 *Int.*, *156*(3), 701-713.

703 Hamiel, Y., Lyakhovsky, V., & Agnon, A., 2005. Rock dilation, nonlinear deformation, and
704 pore pressure change under shear. *Earth and Planetary Science Letters*, *237*(3-4), 577-589.

705 Hamiel, Y, V. Lyakhovsky, S. Stanchits, G. Dresen, and Y. Ben-Zion, 2009. Brittle
706 Deformation and Damage-Induced Seismic Wave Anisotropy in Rocks, *Geophys. J. Int.*, 178,
707 901–909, doi: 10.1111/j.1365-246X.2009.04200.x.

708 Han, B., Xie, S. Y., & Shao, J. F., 2016. Experimental investigation on mechanical behavior
709 and permeability evolution of a porous limestone under compression, *Rock Mechanics and*
710 *Rock Engineering*, 49(9), 3425-3435.

711 Handin, J., Hager Jr, R.V., Friedman, M., & Feather, J.N., 1963. Experimental deformation of
712 sedimentary rocks under confining pressure: pore pressure tests. *AAPG Bulletin*, *47*(5), 717-
713 755.

714 Heap, M. J., Vinciguerra, S., & Meredith, P., 2009. The evolution of elastic moduli with
715 increasing crack damage during cyclic stressing of a basalt from Mount Etna volcano,
716 *Tectonophysics*, 471(1-2), 153–160. https://doi.org/10.1016/j.tecto.2008.10.004.

717 Huang, L., Baud, P., Cordonnier, B., Renard, F., Liu, L., & Wong, T.-F., 2019. Synchrotron
718 X-ray imaging in 4D: Multiscale failure and compaction localization in triaxially compressed
719 porous limestone, *Earth and Planetary Science Letters*, 528,
720 https://doi.org/10.1016/j.epsl.2019.115831.

721 Inglis, C. E., 1913. Stresses in a plate due to the presence of cracks and sharp corners. *Trans.*
722 *Inst. Naval Archit*., 55, 219-241.

723 Irwin, G. R., 1948. Fracture dynamics, Fracturing of Metals. *American Society of Metals*.
724 147-166.

725 Kobchenko, M., Panahi, H., Renard, F., Dysthe, D., Malthe-Sorrenssen, A., Mazzini, A.,
726 Scheibert, J., Jamtveit, B., & Meakin, P., 2011. 4D imaging of fracturing in organic-rich
727 shales during heating. *J. Geophys. Res.: Solid Earth*, 116, B12201.
728 https://doi.org/10.1029/2011JB008565.

729 Kolosov, G., 1909. Sur le probleme plan dans la théorie d'élasticité, *Atti IV Congresso*
730 *Internationale Matematici*, 3, 187-190.

731 Lawn, B., 1993. *Fracture of Brittle Solids*. Cambridge University Press, Cambridge.

732 Lyakhovsky, V., Ben-Zion, Y., & Agnon, A., 1997. Distributed damage, faulting, and
733 friction. *J. Geophys. Res.: Solid Earth*, *102*(B12), pp.27635-27649.

734 Lyakhovsky, V., Hamiel, Y., Ampuero J.-P., & Ben-Zion, Y., 2009. Nonlinear damage
735 rheology and wave resonance in rocks, *Geophys. J. Int.*, 178, 910–920, doi: 10.1111/j.1365-
736 246X.2009.04205.x.

737 Lyakhovsky, V., Hamiel, Y., & Ben-Zion, Y., 2011. A non-local visco-elastic damage model
738 and dynamic fracturing. *Journal of the Mechanics and Physics of Solids*, *59*(9), 1752-1776.

739 Mair, K., Main, I., & Elphick, S., 2000. Sequential growth of deformation bands in the
740 laboratory. *Journal of Structural Geology*, *22*(1), 25-42.

741 Mansfield, C., & Cartwright, J., 2001. Fault growth by linkage: observations and implications
742 from analogue models. *Journal of Structural Geology*, *23*(5), 745-763.

743 McBeck, J.A., Cooke, M.L., Herbert, J.W., Maillot, B., & Souloumiac, P., 2017. Work
744 optimization predicts accretionary faulting: An integration of physical and numerical
745 experiments. *Journal of Geophysical Research: Solid Earth*, *122*(9), 7485-7505

746 McBeck, J. A., Cordonnier, B., Vinciguerra, S., & Renard, F., 2019. Volumetric and shear
747 strain localization in Mt. Etna basalt, *Geophysical Research Letters*, 46(5), 2425-2433.

748 McBeck, J., Kobchenko, M., Hall, S.A., Tudisco, E., Cordonnier, B., Meakin, P., & Renard,
749 F., 2018. Investigating the onset of strain localization within anisotropic shale using digital
750 volume correlation of time-resolved X-ray microtomography images. *J. Geophys. Res.: Solid*
751 *Earth*. https://doi.org/10.1029/2018JB015676.

752 Mitra, G., 1994. Strain variation in thrust sheets across the Sevier fold-and-thrust belt (Idaho-
753 Utah-Wyoming): Implications for section restoration and wedge taper evolution. *Journal of*
754 *Structural Geology*, *16*(4), 585-602.

755 Mohr, O., 1900. Welche Umstande bedingen die Elastizitatsgrenze und den Bruch eines
756 Materials? *Zeit des Ver Deut. Ing.*, 44:1524–1530.

757 Moore, D.E., & Lockner, D.A., 1995. The role of microcracking in shear-fracture propagation
758 in granite. *Journal of Structural Geology*, *17*(1), pp.95-114.

759 Myachkin, V.I., Sobolev, G.A., Dolbilkina, N.A., Morozow, V.N., & Preobrazensky, V.B.,
760 1972. The study of variations in geophysical fields near focal zones of
761 Kamchatka. *Tectonophysics*, *14*, 287-293.

762 Nur, A., 1972. Dilatancy, pore fluids, and premonitory variations of t_s/t_p travel times. *Bulletin*
763 *of the Seismological Society of America*, 62(5), 1217-1222.

764 Paul, B., 1961. A modification of the Coulomb-Mohr theory of fracture. *Journal of Applied*
765 *Mechanics*, *28*(2), 259-268.

766 Peacock, D.C.P., Sanderson, D.J., & Rotevatn, A., 2018. Relationships between
767 fractures. *Journal of Structural Geology*, *106*, 41-53.

768 Peng, S., & Johnson, A.M., 1972, January. Crack growth and faulting in cylindrical
769 specimens of Chelmsford granite. In *International Journal of Rock Mechanics and Mining*
770 *Sciences & Geomechanics Abstracts* (Vol. 9, No. 1, pp. 37-86). Pergamon.

771 Petit, J.P., & Barquins, M., 1988. Can natural faults propagate under mode II
772 conditions?. *Tectonics*, *7*(6), pp.1243-1256.

773 Reches, Z.E. & Lockner, D.A., 1994. Nucleation and growth of faults in brittle rocks. *J.*
774 *Geophys. Res.: Solid Earth*, 99(B9), 18159-18173.

775 Renard, F., 2017. Critical evolution of damage towards system size failure in a crystalline
776 rock [Data set]. *Norstore*. https://doi.org/10.11582/2017.00025.

777 Renard, F., 2018a. Volumetric and shear strain localization in Mt. Etna basalt [Data set].
778 *Norstore*. https://doi.org/10.11582/2018.00036

779 Renard, F., 2018b. Dynamic in situ three-dimensional imaging and digital volume correlation
780 analysis quantify strain localization and fracture coalescence in sandstone [Data set].
781 *Norstore*. https://doi.org/10.11582/2018.00022

782 Renard, F., 2018c. Volumetric and shear processes in crystalline rock during the approach to
783 faulting [Data set]. *Norstore*. https://doi.org/10.11582/2018.00023

784 Renard, F., Cordonnier, B., Dysthe, D.K., Boller, E., Tafforeau, P., & Rack, A., 2016. A
785 deformation rig for synchrotron microtomography studies of geomaterials under conditions
786 down to 10 km depth in the earth, *Journal of Synchrotron Radiation*, 23 (4), 1030–1034.

787 Renard, F., Cordonnier, B., Kobchenko, M., Kandula, N., Weiss, J., & Zhu, W., 2017.
788 Microscale characterization of rupture nucleation unravels precursors to faulting in
789 rocks. *Earth and Planetary Science Letters*, *476*, 69-78.

790 Renard, F., & McBeck, J., 2018. Investigating the onset of strain localization within
791 anisotropic shale using digital volume correlation of time-resolved X-ray microtomography
792 images (data set). *Norstore*. https://doi. org/10.11582/2018.00005.

793 Renard, F., McBeck, J., Cordonnier, B., Zheng, X., Kandula, N., Sanchez, J.R., Kobchenko,
794 M., Noiriel, C., Zhu, W., Meakin, P., & Fusseis, F., 2019a. Dynamic in situ three-dimensional

imaging and digital volume correlation analysis to quantify strain localization and fracture coalescence in sandstone. *Pure and Applied Geophysics*, *176*(3), 1083-1115.

Renard, F., McBeck, J., Kandula, N., Cordonnier, B., Meakin, P., & Ben-Zion, Y., 2019b. Volumetric and shear processes in crystalline rock approaching faulting. *Proceedings of the National Academy of Sciences*, *116*(33), 16234-16239.

Rice, J. R., 1980. The mechanics of Earthquake Rupture, in *Physics of the Earth's Interior*, eds. A. M. Dziewonski and E. Boschi, 555-649, Italian Physical Society / North Holland, Amsterdam.

Rice, J. R., & Rudnicki, J. W., 1980. A note on some features of the theory of localization of deformation. *International Journal of Solids and Structures*, 16(7), 597-605.

Rodríguez, P., & Celestino, T. B., 2019. Application of acoustic emission monitoring and signal analysis to the qualitative and quantitative characterization of the fracturing process in rocks. *Engineering Fracture Mechanics*, 210, 54-69.

Rudnicki, J. W., & Rice, J. R., 1975. Conditions for the localization of deformation in pressure-sensitive dilatant materials, *Journal of the Mechanics and Physics of Solids*, 23(6), 371-394.

Rutter, E. H., & Neumann, D. H. K., 1995. Experimental deformation of partially molten Westerly granite under fluid-absent conditions, with implications for the extraction of granitic magmas, *J. Geophys. Res.: Solid Earth*, 100(B8), 15697-15715.

Ben-Zion, Y. and C. G. Sammis, 2003. Characterization of Fault Zones, *Pure Appl. Geophys*., 160, 677-715.

Stanchits, S., Vinciguerra, S., & Dresen, G., 2006. Ultrasonic velocities, acoustic emission characteristics and crack damage of basalt and granite, *Pure and Applied Geophysics*, 163(5-6), 975-994.

Storti, F., Salvini, F. and McClay, K., 1997. Fault-related folding in sandbox analogue models of thrust wedges. *Journal of Structural Geology*, *19*(3-4), 583-602.

Tal, Y., Evans, B., & Mok, U., 2016. Direct observations of damage during unconfined brittle failure of Carrara marble. *J. Geophys. Res.: Solid Earth*, 121(3), 1584-1609.

Tudisco, E., Andò, E., Cailletaud, R., & Hall, S.A., 2017. TomoWarp2: a local digital volume correlation code. *SoftwareX*, 6, 267–270.

Vinciguerra, S., Trovato, C., Meredith, P. G., & Benson, P. M., 2005. Relating seismic velocities, thermal cracking and permeability in Mt. Etna and Iceland basalts, *International Journal of Rock Mechanics and Mining Sciences*, 42(7–8), 900–910. https://doi.org/10.1016/j.ijrmms.2005.05.022

Wong, R.H., & Chau, K.T., 1998. Crack coalescence in a rock-like material containing two cracks. *International Journal of Rock Mechanics and Mining Sciences*, *35*(2), 147-164.

Wong, T. F., David, C., & Zhu, W., 1997. The transition from brittle faulting to cataclastic flow in porous sandstones: Mechanical deformation, *J. Geophys. Res.: Solid Earth*, 102(B2), 3009-3025.

Zhao, X.G., & Cai, M., 2010. A mobilized dilation angle model for rocks. *International Journal of Rock Mechanics and Mining Sciences*, *47*(3), 368-384.

Zhu, W., Baud, P. & Wong, T.F., 2010. Micromechanics of cataclastic pore collapse in limestone. *J. Geophys. Res.: Solid Earth*, *115*(B4).

839 **Table 1**

840 Experimental conditions, materials, dimension of rock cores and numbers of X-ray

841 tomograms acquired in twelve rock deformation experiments.

rock type	experiment code	confining stress (MPa)	sample diameter (mm)	# of X-ray tomograms
Fontainebleau sandstone	FBL01	20	5	184
	FBL02	10	5	47
Mount Etna basalt	ETNA01	10	4	32
	ETNA02	10	4	36
monzonite	MONZ04	35	4	65
	MONZ05	25	4	80
Westerly granite	WG02	5	4	30
	WG04	10	4	66
Green River shale	GRS02	20	5	60
	GRS03	20	5	61
Anstrude limestone	ANS02	20	5	41
	ANS05	5	5	26

842

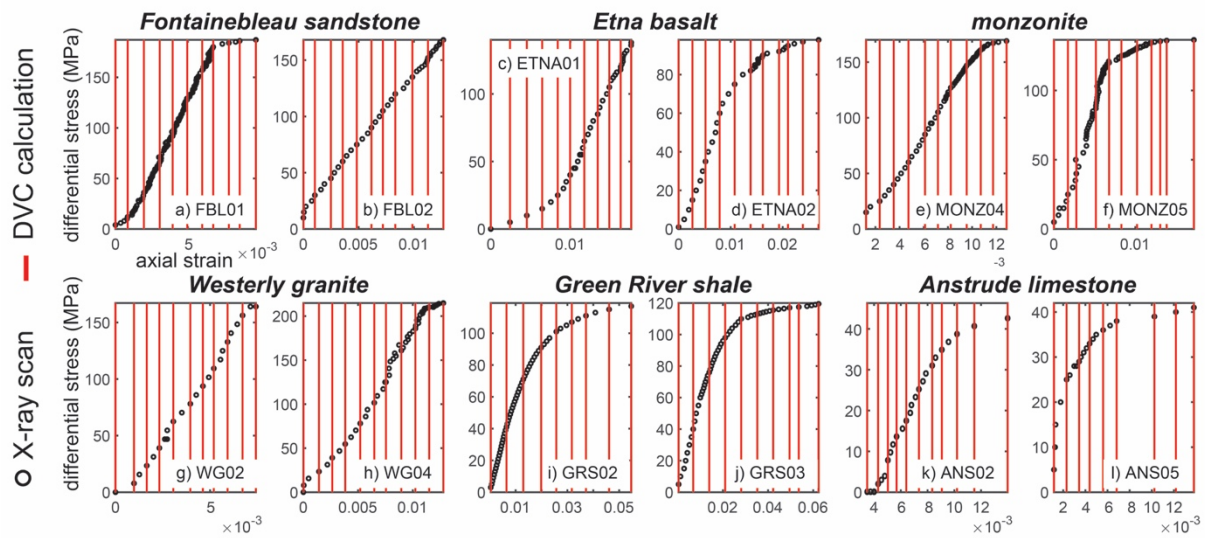

843 **Figure 1**

844 Loading history of experiments on Fontainebleau sandstone (a-b), Mount Etna basalt (c-d),
845 monzonite (e-f), Westerly granite (g-h), Green River shale (i-j), and Anstrude limestone (k-l).
846 Black dots indicate the axial strain and differential stress conditions when an *in situ* X-ray
847 tomogram is acquired. Red lines indicate the loading conditions of the tomograms used in the
848 DVC calculations. The pairs of tomograms used in the DVC calculation are separated by
849 approximately constant amounts of macroscopic axial strain in each experiment.

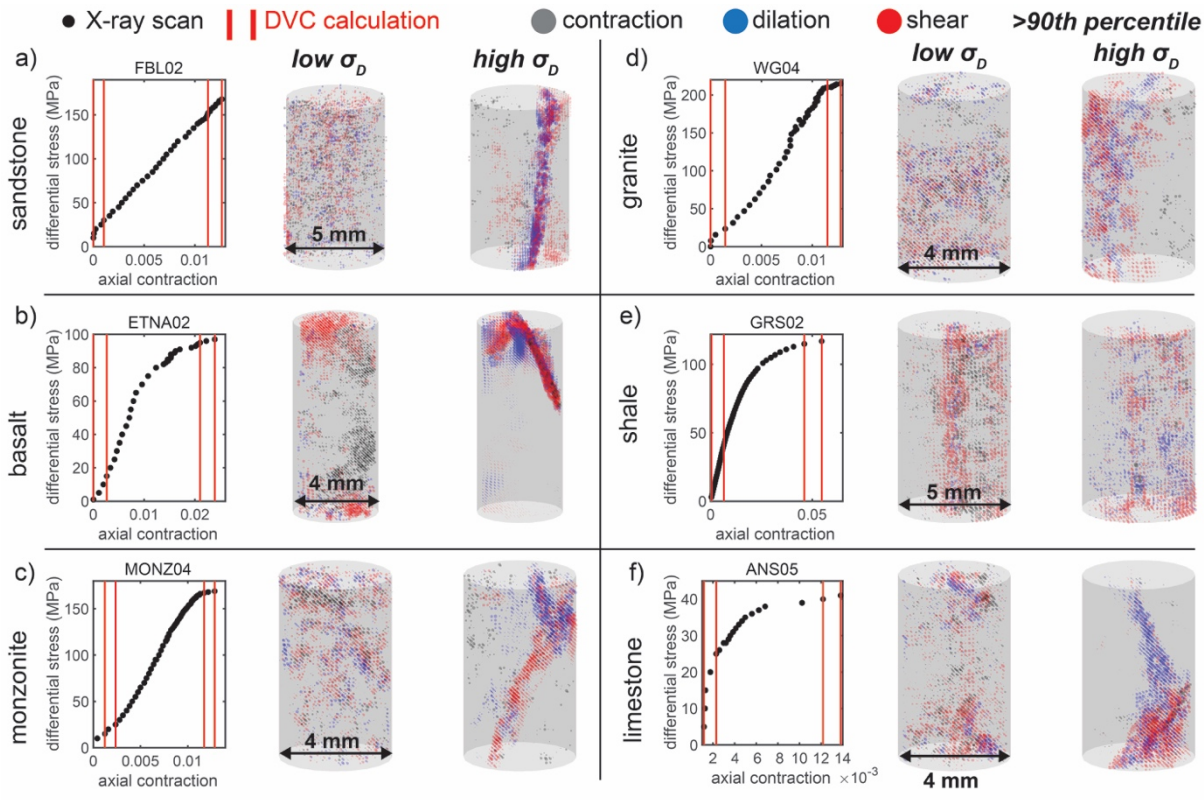

850

851 **Figure 2**

852 Snapshots of the 3D strain fields at low and high differential stress, σ_D, for experiments on
853 sandstone (a), basalt (b), monzonite (c), granite (d), shale (e), and limestone (f). The plots show
854 the stress-strain conditions of each acquired tomogram (black dots), and the conditions of the
855 DVC calculations (red lines). Black, blue and red dots in the gray cylindrical cores show where
856 the contraction, dilation and shear strain exceed the 90th percentile of the corresponding strain
857 population, respectively.

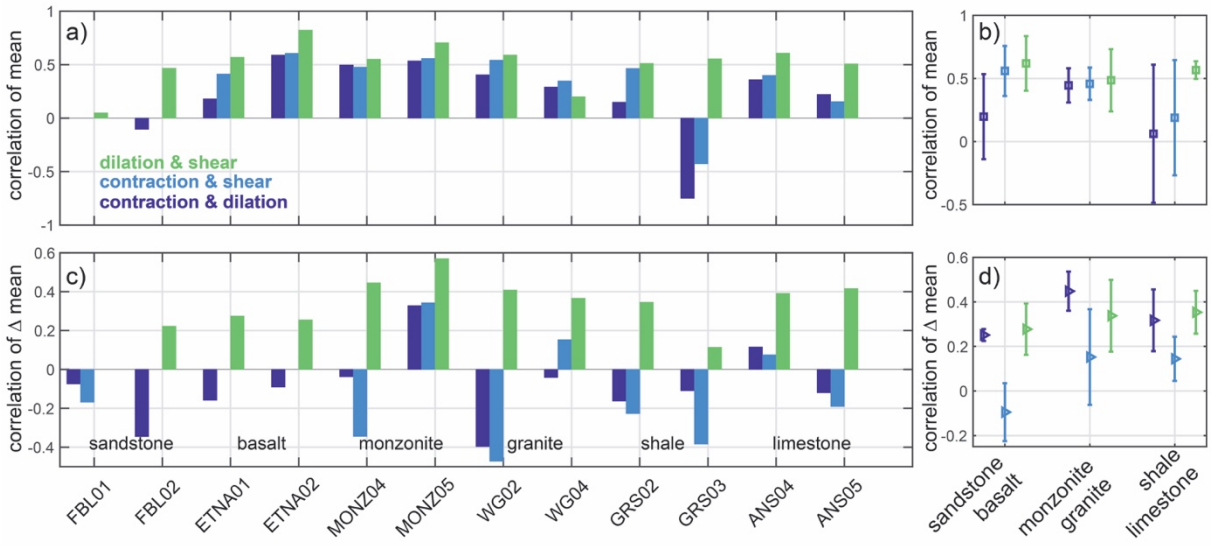

858

859 **Figure 3**

860 Correlation coefficients between the strain component means (a-b) and change in the strain
861 component means (c-d) at subvolumes throughout each experiment. Correlation between 1) the
862 dilation and shear strain, 2) contraction and shear strain, and 3) contraction and dilation shown
863 with 1) green, 2) light blue, and 3) dark blue, respectively. b, d) Mean ± one standard deviation
864 of the correlation coefficient between the magnitude of the strain means (b) and change in strain
865 means (d) for each of the four experiments on sandstone and basalt, monzonite and granite, and
866 shale and limestone.

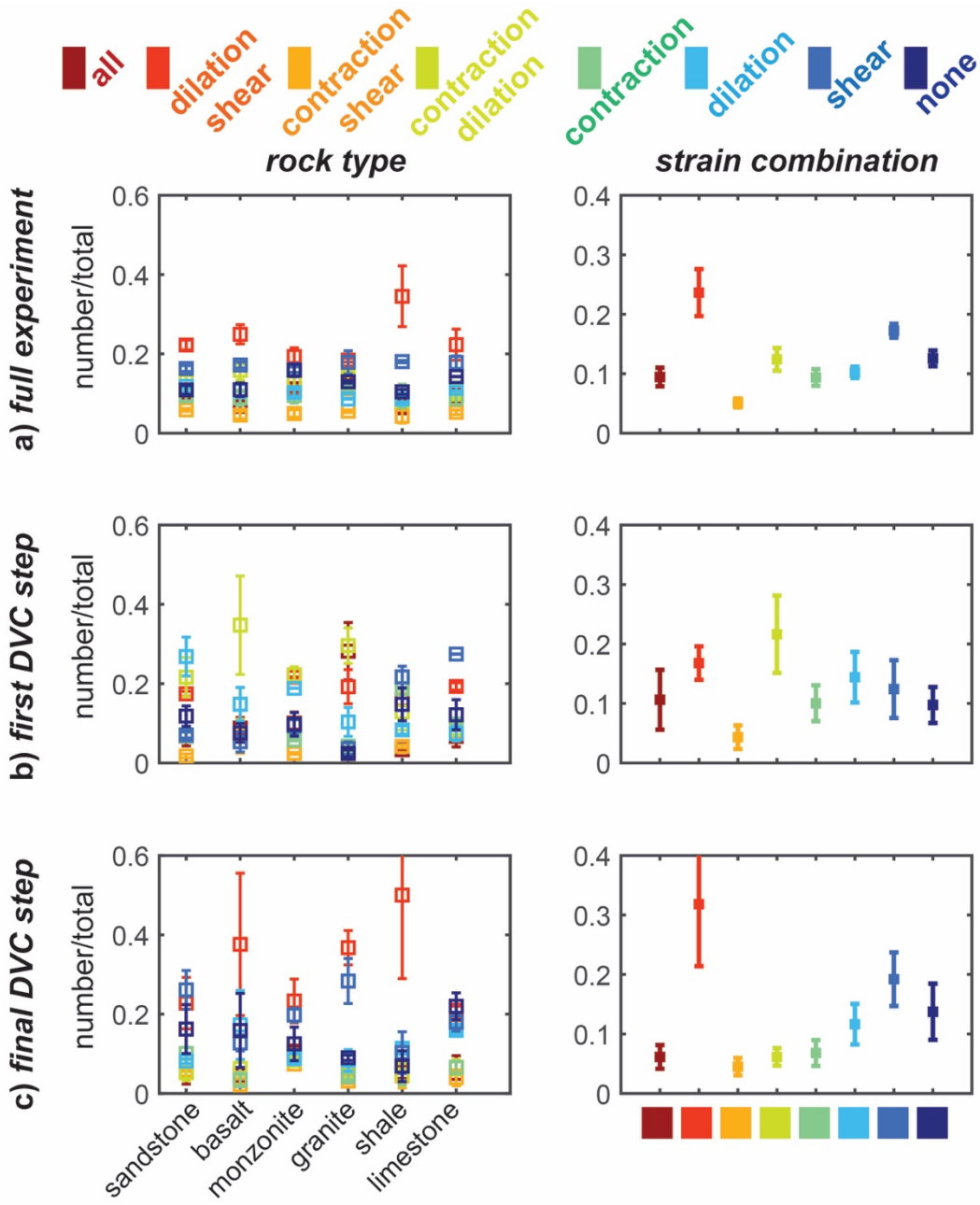

867 **Figure 4**

868 Summary of the differences in strain accommodation modes at different stages of loading: a)
869 throughout the full experiment, b) first DVC calculation, and c) final DVC calculation. Left:
870 mean ± one standard deviation of the normalized strain accommodation frequency, n/t, of the
871 two experiments of each rock type. n/t is measured as the number of voxels occupied by the
872 increase in none, all, one, or two of the strain components, n, out of the total number of voxels,
873 t. Right: mean ± one standard deviation of n/t for all the experiments.

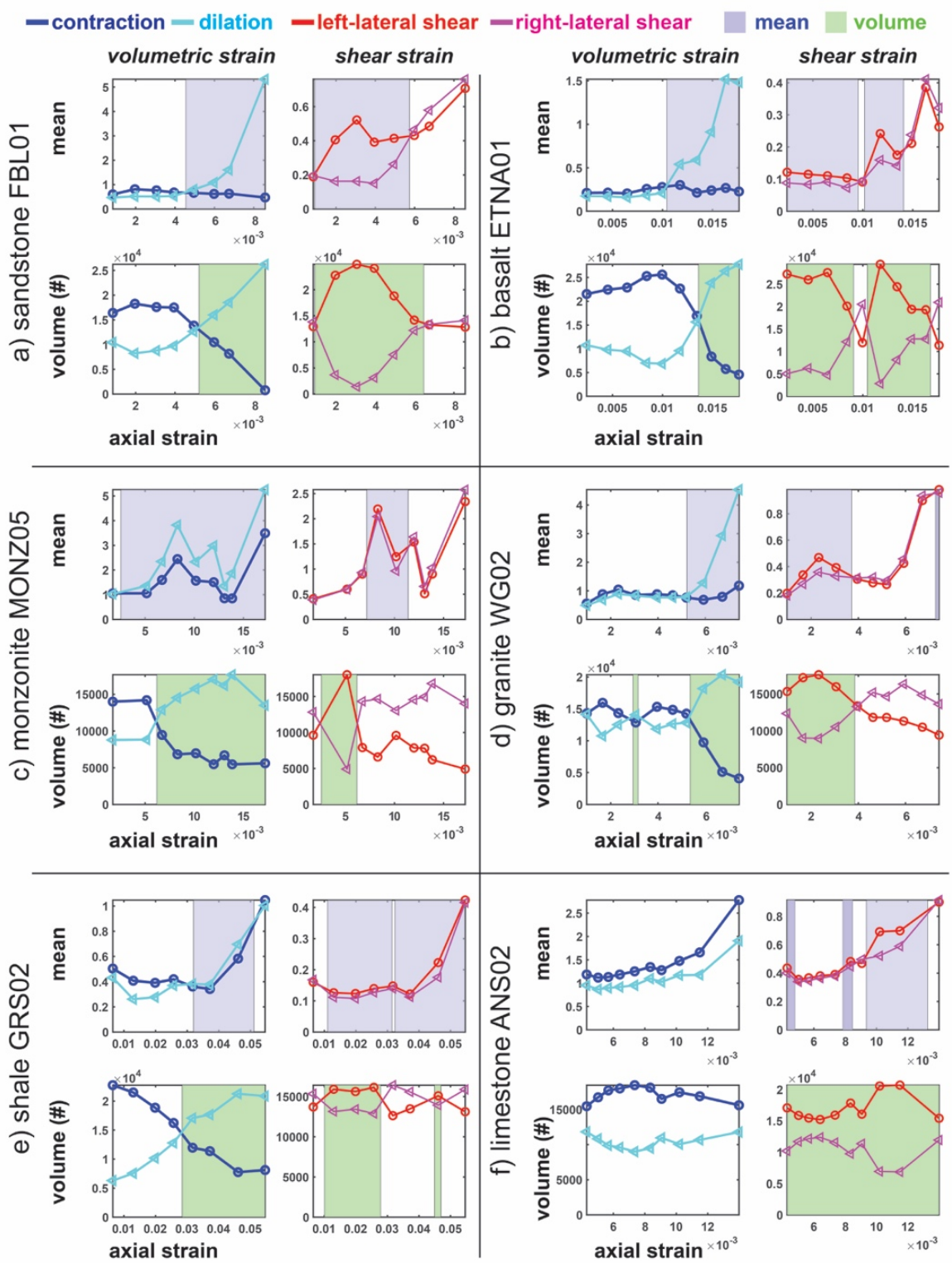

874 **Figure 5**

875 Evolution of strain accommodation throughout time (macroscopic axial strain) in six
876 experiments on a) sandstone, b) basalt, c) monzonite, d) granite, e) shale and f) limestone. First
877 row of each subsection shows the mean of the strain components, including the dilation,
878 contraction, left-lateral and right-lateral shear strain. Second row shows the volume of the rock

879 that each strain component occupied as the number of voxels. Left and right columns of each
880 subsection show the dilation (light blue) and contraction (dark blue), and left-lateral (red) and
881 right-lateral (pink) shear strain, respectively. Blue and green rectangles highlight the time when
882 the dilation mean (blue) or volume (green) exceeds the contraction mean or volume, and when
883 the left-lateral shear strain mean or volume exceeds the right-lateral shear strain mean or
884 volume, respectively. **Figure** S4 shows these data for the other six experiments.

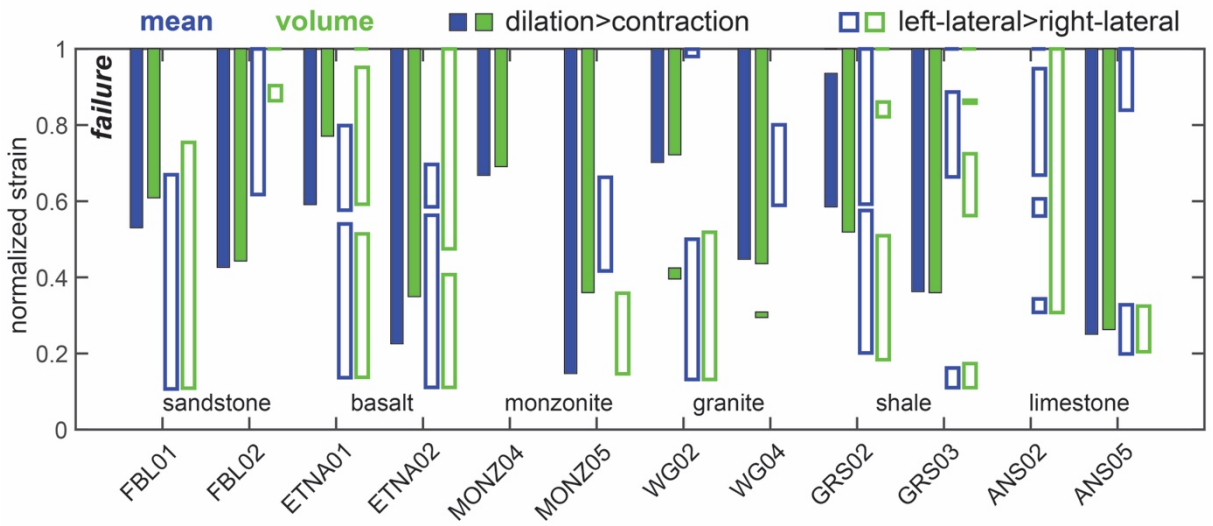

885 **Figure 6**

886 Time periods during each experiment when the mean or volume of the dilation exceeds the
887 contraction, or when the mean or volume of the left-lateral shear strain exceeds the right-lateral
888 shear strain. Time is reported as the normalized strain: the axial strain divided by the axial strain
889 immediately preceding macroscopic failure, with zero at the onset of loading and one at failure.
890 Time periods that correspond to the mean and volume of the strain components shown with
891 blue and green, respectively. Time periods that correspond to the volumetric strains and shear
892 strains shown with filled rectangles and outlines of rectangles, respectively. The mean and
893 volume of the dilation exceeds the contraction by the end of the experiment in eleven of twelve
894 experiments. Near the axial strain when the dilation mean exceeds the contraction mean, the
895 dilation volume also exceeds the contraction volume. This synchronicity of the mean and
896 volume identified for the volumetric strains does not occur for the shear strain components.
897 Dilation tends to delocalize while gaining strength (increasing in mean and volume at the same
898 time), whereas shear strain tends to localize or remain at similar volumes while gaining strength
899 (increasing in mean, but not in volume, or vice versa).

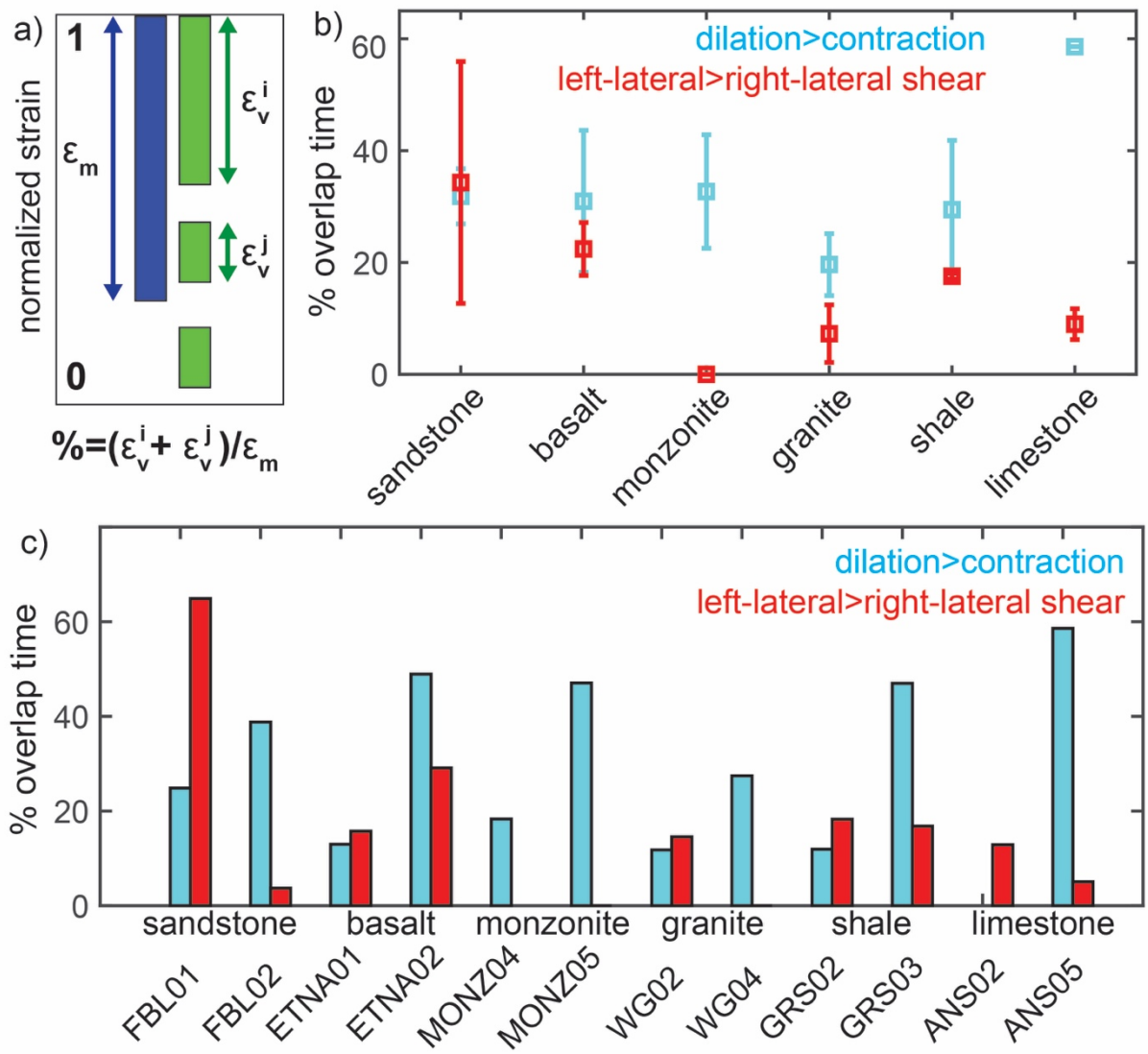

Figure 7

Percent of overlap time when both the mean and volume of a strain component (dilation or left-lateral shear strain) exceeds the other strain component (contraction or right-lateral shear strain). a) Sketch of quantities used to calculate percent overlap time, using the range of normalized axial strain when the mean, ε_m, and volume, ε_v, of a strain component exceeds the other strain component. Percent overlap time for rock types as the mean $\pm$ one standard deviation of each pair of experiments (b), and for individual experiments (c) when the dilation exceeds the contraction (blue) and left-lateral shear strain exceeds the right-lateral shear strain (red). The percent overlap time of the volumetric strains tends to be larger than the percent overlap time of the shear strains.

Figure 8

Correlation length of each strain component throughout loading in six example experiments. **Figure** S5 shows the distribution of the correlation coefficient with distance for each of these experiments, and the correlation length. In some experiments, the correlation length increases with loading, while in other experiments the correlation length decreases or remains similar.

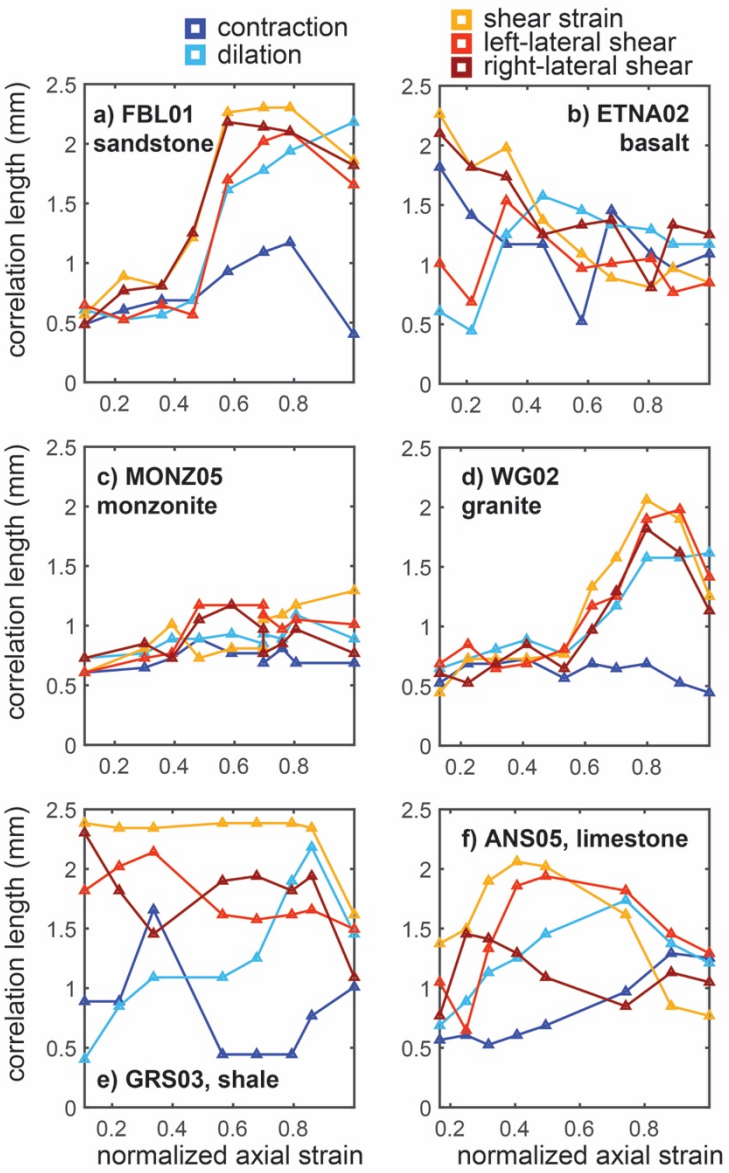

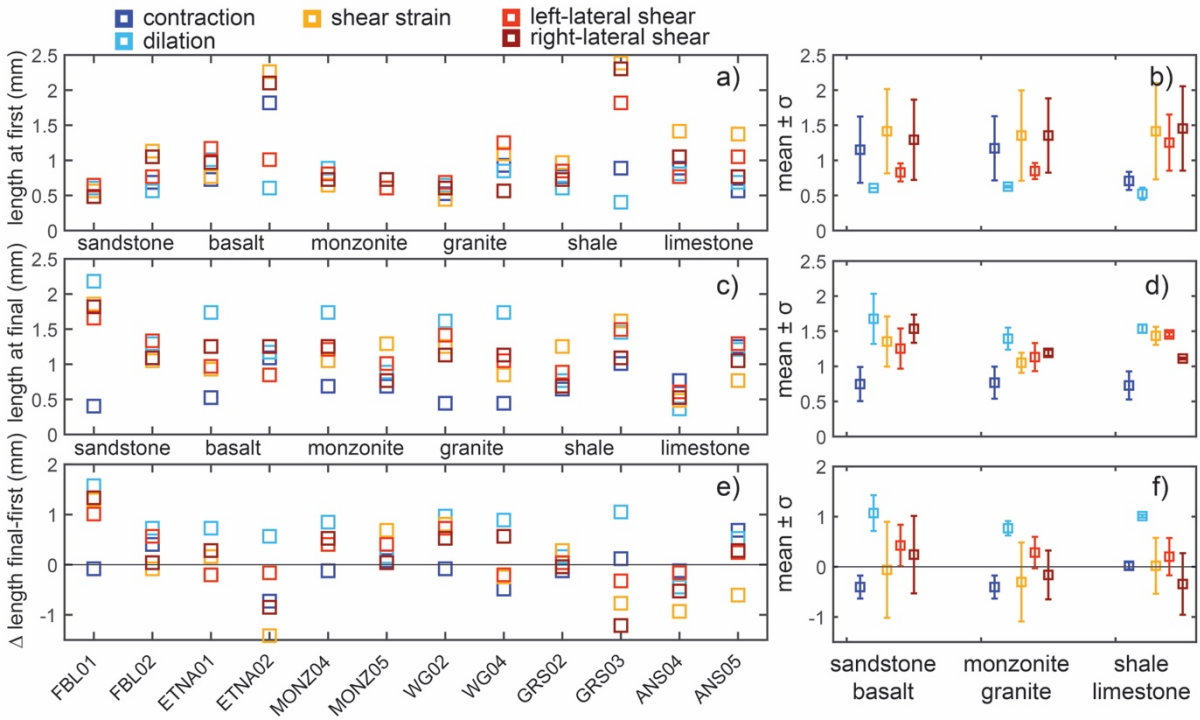

925

926 **Figure 9**

927 Evolution of the correlation length of strain components in each experiment (a, c, e) and as
928 averages of groups of experiments on similar rock types (b, d, f). Correlation length at the first
929 (a, b) and final (c, d) DVC calculations. e, f) Difference in the lengths between the first and
930 final DVC calculations. In the first calculation, under lower differential stress (a, b), the dilation
931 tends to have the lowest correlation length of the strain components. Under higher differential
932 stress (c, d), the dilation tends to have the highest correlation length of the strain components.
933 Consequently, the dilation correlation length tends to increase by the largest magnitudes (e, f).
934 These trends are consistent among the six rock types, and groups of rock types.

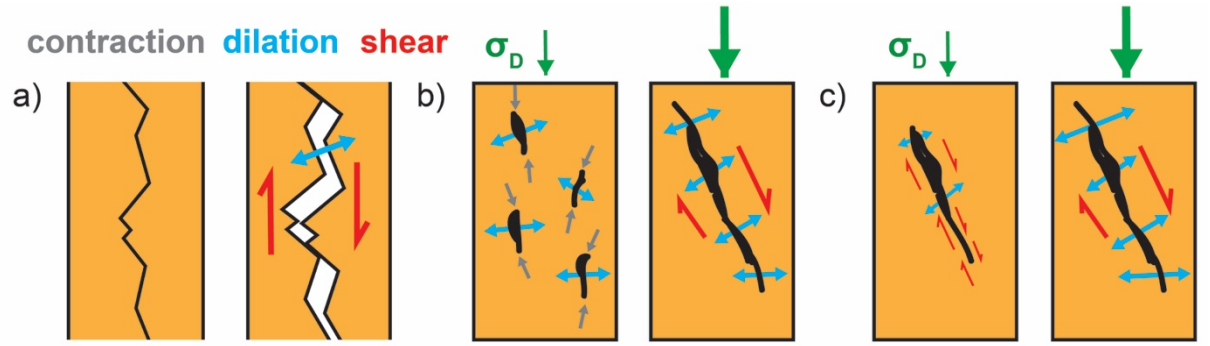

Figure 10

Schematic representation of the strain accumulation and localization process. a) To accommodate shear strain (red arrows) along rough fractures, portions of the fracture surfaces must dilate (blue arrows). b) Under lower differential stress (left), the paired increase in contraction and dilation dominates deformation. b) Under higher differential stress (right), the paired increase in dilation and shear strain dominates deformation. c) The diverging behavior of the strain localization and accumulation process of volumetric and shear strains. Increases in the magnitude of dilation (shown with the thickness of blue arrows) are paired with increases in the volume of rock experiencing dilation (shown with the number of blue arrows). In contrast, increases in the magnitude of shear strain (shown with the thickness of red arrows) are not often paired with increases in the volume of rock experiencing shear strain (shown with the number of red arrows). The correlation length of dilation tends to increase from lower to higher differential stress. In contrast, the correlation length of shear strain does not systematically increase or decrease across all twelve experiments.